ELSEVIER

Thermochimica Acta 266 (1995) 257–275

thermochimica acta

A differential scanning calorimetric study of precipitation in Cu–2Be ☆

A. Varschavsky *, E. Donoso

Universidad de Chile, Facultad de Ciencias Físicas y Matemáticas, Instituto de Investigaciones y Ensayes de Materiales, Plaza Ercilla 883, Casilla 1420, Santiago, Chile

Abstract

Beryllium precipitation from the Cu-rich matrix in a Cu–2 wt% Be alloy homogenized and quenched from 1073 K was studied by differential scanning calorimetry (DSC). The DSC traces showed two main exothermic effects, A and B, each comprising two sub-effects A_1, A_2, and B_1, B_2 respectively. Effects A_1 and A_2 correspond to the precipitation of GP zones and subsequent overlapping and independent precipitation of γ''-phase. Only at very low heating rates can γ'' be inherited from GP zones. Effects B_1 and B_2 correspond to heat evolved during transitions to the states with γ'- and γ-phases respectively. Heat effect A can be quantitatively described in terms of solid solubilities before and after precipitation, and of precipitation heats of the phases involved. The heat content of the combined GP zone/γ''-phase precipitation effect was proportional to the beryllium atoms precipitated, yielding an average value of 21 kJ mol^{-1} beryllium for beryllium precipitation. It was shown that γ'-phase arises from the combined transition from states with GP zones and γ''-phases, whereas γ arises from the transition of states with γ'' and γ'. The apparent activation energies associated with GP zones, and γ'', γ'- and γ-phases are 0.94 ± 0.07, 1.26 ± 0.07, 1.31 ± 0.08 and 1.69 ± 0.1 eV respectively. These values are discussed in terms of dissolved atom mobility related to vacancy concentration, and the direction of plate-like precipitate growth (either normal or perpendicular to the plate). Small discontinuous precipitations of γ-phase occurred along with the transformation to the state with γ'-phase.

Keywords: Beryllium; Copper; DSC; Precipitation

* Corresponding author.

☆ Dedicated to Hiroshi Suga on the Occasion of his 65th Birthday.

SSDI 0040-6031(95)02338-0

1. Introduction

The excellent age-hardenability and high electrical conductivity of Cu–Be alloys have been used extensively, e.g. for springs, diaphragms, bearings, and non-sparking tools. In this alloy system the precipitation sequence from the supersaturated solid solution includes at least four stages [1–4], namely

$$\text{Solid solution} \rightarrow \text{GP zones} \rightarrow \gamma'' \rightarrow \gamma' \rightarrow \gamma$$

where GP zones are multilayer plates that form coherently on {100} matrix planes, γ'' is a metastable phase with a monoclinic structure, γ' is also metastable with a bcc structure and γ precipitates have equilibrium bcc structure [4].

Furthermore, it has been shown that GP zones are not the least stable of metastable phases in the Cu–Be system, since at room temperature equiaxed Be-enriched zones have been observed to precede their formation [4–8]. The precipitation process in these alloys can be regarded [9] as an isostructural decomposition of the f.c.c. phase into Be-rich and Be-depleted regions, followed by the transformation of the Be-enriched f.c.c. regions into Be-enriched bcc regions via Bain strain in concomitance with atomic order, to form the B2 structure. The morphology and structure of γ''- and γ'-phases are interpreted as constrained states of the same precipitated Be phase γ with different habit planes [9]. In line with these results, it has also been recently suggested [10, 11] that GP zones, and the γ''- and γ'-phases transform continuously to the subsequent phase during an isothermal ageing treatment.

The above precipitation sequence has been studied extensively, with a wide variety of interpretations regarding morphology, crystallography and habit planes of the several intermediate phases formed prior to the equilibrium γ-phase. In addition to continuous precipitation, cells of discontinuous precipitation advance from grain boundaries into the grain centres where continuous precipitation occurred [12–14]. The precipitation sequence for simultaneous continuous and discontinuous modes, recently studied [15], is sensitive to heat treatment. For instance γ''-phase is absent in a directly quenched (to 623 and 673 K) and aged Cu–2Be alloy [4]. Experimental work has been done up to now under isothermal conditions and thus scarce literature exists regarding the anisothermal precipitation stages [10, 16, 17].

This paper studies the influence of the heating rate on the precipitation effects in a quenched Cu–2Be alloy, and its main objectives are: (a) to discriminate the anisothermal precipitation sequence using enthalpimetric calculations; (b) to evaluate the different precipitation stages as a function of heating rate; (c) to elucidate the origin (nucleation and growth or transition) of these stages; and (d) to provide kinetic data affording a deeper insight into the atomic mechanisms of the decomposition process.

As Be precipitation from a Cu-rich matrix involves enthalpy changes large enough to allow differential scanning calorimetry (DSC), this technique was used in this work.

2. Material and experimental procedure

The material investigated was a polycrystalline Cu–2 wt% Be alloy received as 150 × 150 mm square plates, 1.0 mm thick.

Microcalorimetric analysis of the samples was performed in a Dupont 2000 thermal analyser. Specimen discs, 1.0 mm thick and 6 mm in diameter, were prepared using a spark-cutter machine. The samples were solubilized at 1073 K for 3 h, water-quenched and stored at room temperature for 2 h prior to DSC measurements of the heat flow by operating the calorimeter in the constant-heating mode (heating rates of 0.833, 0.500, 0.333, 0.167 and 0.082 K s^{-1}). To increase measurement sensitivity, a high-purity, well annealed copper disc of mass approximately equal to that of the sample in which no thermal events occur over the temperature range scanned was used as a reference in each case. Both reference and specimen were enclosed in an aluminium pan sealed with an aluminium cover. To minimize oxidation, dried nitrogen was passed through the calorimeter (0.8×10^{-4} m^3 min^{-1}).

Runs were recorded between 300 and 880 K. Because beyond approx. 800 K (depending on heating rate) only heat effects corresponding to dissolution were observed in the DSC traces, in this precipitation study only the 300–800 K interval was analysed. After the first run each specimen was maintained at 880 K for 5 min and allowed to cool freely in the calorimeter for 3 h yielding cooling curves that were very similar and nearly exponential. It was observed that the cooling rate was 0.417 K s^{-1} at 880 K, and 0.117 K s^{-1} below 560 K. When room temperature was reached, a second run at the same heating rate was made using each specimen. The DSC traces presented in this work were obtained by subtracting the baseline from the first run. This baseline represents the temperature-dependent heat capacity of the alloy in the existing thermal conditions, and its value was in agreement with the Kopp–Neumann rule. Afterwards, the resulting traces were converted into a differential heat capacity versus temperature curve. The heat-capacity remainder, namely the differential heat capacity ΔC_p, represents the heat associated with solid state reactions during the DSC run. Thus reaction peaks in the ΔC_p versus T curve can be characterized by the reaction enthalpy of a particular event. The DSC curves presented in this work are all such rerun-corrected curves.

3. Results and discussion

3.1. DSC thermograms

Fig. 1 shows DSC runs at various heating rates ϕ. Since no exothermic heat flow occurs during a second run, this means that, after the first run, precipitation proceeds completely during cooling. Thus the curves obtained by subtracting the second run from the first reflect only the heat flow difference due to the free enthalpy difference just before the runs.

The DSC traces show two main effects, A and B, comprising sub-effects A_1, A_2, and B_1, B_2 respectively. Because the heat flow in all traces just before the first run is higher than before the second run (the matrix of a quenched specimen is supersaturated), the four sub-effects observed in the rerun-corrected curves will be generally exothermic. Therefore, the exothermic effects A_1, A_2, and B_1, B_2 are interpreted as follows. Effect A_1 is related to GP zone formation, while effect A_2 is related to γ''-phase precipitation.

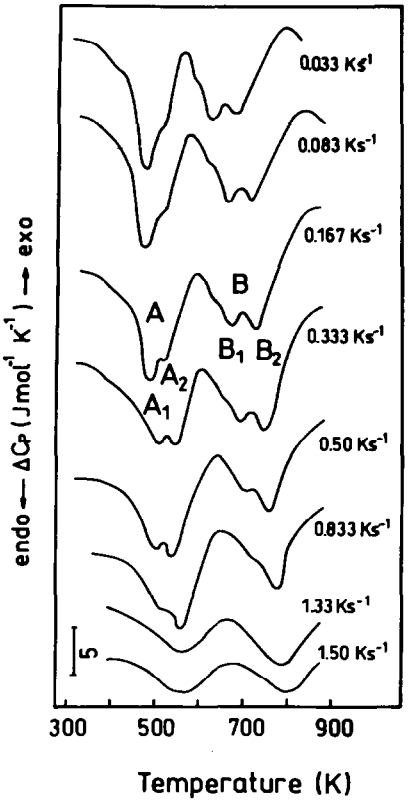

Fig. 1. DSC traces for quenched Cu–2Be. Heating rates ϕ and the two main effects A and B (comprising subeffects A_1, A_2, and B_1, B_2) are shown.

Effect B_1 is associated with the GP zone and γ''-phase transformations to a state with γ' precipitates; effect B_2 is associated with γ''- and γ'-phase transformations into γ-phase. These interpretations will be discussed in the next section. As the DSC heating-rate increased, the effects shifted to higher temperatures, effects A_1 and B_1 tend to disappear, and then the prevailing thermal events correspond to A_2 and B_2. An overlapping of events A_1, A_2 and of B_1, B_2 takes place at all heating rates.

All heat contents were determined by measuring the area between the rerun-corrected DSC curves. In the case of overlapping effects A_1, A_2, and B_1, B_2 the respective heat contents were obtained by a deconvolution process based on a heat flow extrapolation of effects A_1, A_2, and B_1, B_2 at the temperatures at which these effects coexisted. It is worth recalling that the end-temperature ranges of these effects lie within those of the GP zones, and γ''-, γ'- and γ-phases, in line with literature results [1, 2, 4, 11, 13, 18] for all the heating rates employed herein.

Table 1 shows the initial, peak and end temperatures T_o, T_p and T_e respectively, together with the heat content ΔH of all peaks. It can be observed that with increasing

Table 1
The initial, peak and end temperatures of effects A_1, A_2, B_1, B_2 and the respective heat contents in quenched Cu–2Be as a function of differential scanning calorimetry at heating rate ϕ. Values for heat contents ΔH_A and ΔH_B are also given

Thermal event	T(K) ΔH/(J mol^{-1})	ϕ/(K s^{-1})							
		0.033	0.083	0.167	0.333	0.50	0.833	1.333	1.5
A_1	T_o	315	323	333	346	358	365	–	–
	T_p	468	470	478	490	500	509	–	–
(GP)	T_e	525	583	550	563	575	581	–	–
	$-\Delta H_{A1}$	714	688	677	620	540	406	–	–
A_2	T_o	453	460	430	478	489	496	–	–
	T_p	507	513	522	531	540	553	–	–
	T_e	543	560	572	592	614	635	653	660
(γ'')	$-\Delta H_{A2}$	376	394	404	435	490	556	597	502
	$-\Delta H_A$	1090	1082	1075	1055	1030	962	597	502
B_1	T_o	581	588	601	620	650	677	–	–
	T_p	622	639	651	671	686	711	–	–
(γ')	T_e	703	719	727	748	755	761	–	–
	$-\Delta H_{B1}$	501	470	447	411	312	209	–	–
B_2	T_o	638	643	653	665	683	701	–	–
	T_p	688	701	713	726	739	757	–	–
	T_e	713	730	746	776	796	820	828	831
(γ)	$-\Delta H_{B2}$	379	403	419	441	463	501	510	460
	$-\Delta H_B$	880	873	866	852	775	710	510	460

heating rate, the heat contents ΔH_{A1} and ΔH_{B1} decreased and the heat contents ΔH_{A2} and ΔH_{B2} increased. The characteristic temperatures also increased with increasing heating rate. In addition, the ΔH_A and ΔH_B of the composite peaks always decreased with increasing heating rate. The relationship between thermal events A_1 and A_2 is such that A_1 decreases as A_2 increases with heating rate, so that combined precipitation of GP zones and γ'' takes place at low and medium heating rates. With increasing heating rates, the precipitated amount of GP zones decreased, but as precipitation proceeds, an increased amount of γ'' nucleated and grew. GP-zone formation becomes less important (even disappearing) as heating rate is increased, because the annihilation rate of excess vacancies at these heating rates must be much larger than the maximum annihilation rates compatible with GP-zone formation. Since the heat contents of thermal effects A_1 and A_2 vary inversely, GP and γ'' nucleate independently. As shown in subsequent sections, the decrease in heat content of effect B_1 associated with γ' is related to the decrease in heat content of the GP zones when heating rate is increased. At low and high temperatures, the global heat events ΔH_A and ΔH_B decreased with increasing heating rate because they exhibit heat effects (composites in this case) normally observed in non-isothermal precipitation phenomena [19]. Therefore, as precipitation reactions are usually controlled by diffusion, an increase in DSC heating rate results in an increase in precipitation temperatures and causes a two-fold effect: (1)

the amount of precipitated atoms decrease due to increased solid solubilities at increased precipitation temperatures; and (2) the proportion of phases stable at high temperatures in the precipitating phases increases.

3.2. *Precipitation phenomena observed for effect A*

It is thought that effect A can be understood as a result of the combined precipitation of GP and γ''. To identify such events, the theoretical calculation of heat evolution during the precipitation of GP zones and γ'' are required separately, assuming that, at the end temperatures of effects A_1 and A_2, no precipitation of the respective phases is taking place, i.e. the composition of the Cu-rich matrix is given by the solid solubilities for GP zones and γ''-phase at the end of each thermal effect [19, 20], namely $C_M^{GP}(T_e^{GP})$ and $C_M^{\gamma''}(T_e^{\gamma''})$. This is equivalent to saying that a dynamic equilibrium state exists for the phase at the end temperature [21–23].

The total precipitation heat for GP zones and γ'' can be calculated separately considering: (a) the precipitated Be atoms in GP zones and γ''-phase, and (b) their respective heat of precipitation, as follows. For GP zones after precipitation, the mole fraction of the Cu-rich matrix is given by $C_M^{GP}(T_e^{GP})$, and the precipitation reaction is then

$$Cu_{[1-\bar{c}]}Be_{[\bar{c}]} \rightarrow m\,Cu_{[1-c_M^{GP}(T_e^{GP})]} + Be_{[c_M^{GP}(T_e^{GP})]} + p\,Be$$

where m and p represent the number of moles of Cu-rich phase and GP zones, respectively, the latter being considered as a first approximation for those formed by the Be plates [4, 9]; $\bar{c}$ represents the initial Be concentration of the alloy.

Conservation of mass requires for copper

$$1-\bar{c} = m[1-c_M^{GP}(T_e^{GP})] \tag{1}$$

and for beryllium

$$\bar{c} = mc_M^{GP}(T_e^{GP}) + p \tag{2}$$

so that

$$m = \frac{1-\bar{c}}{1-c_M^{GP}(T_e^{GP})} \tag{3}$$

By combining Eqs. (2) and (3), the value of p can be calculated after neglecting the term $\bar{c}.c_M(T_e^{GP})$

$$p = \frac{\bar{c}-c_M^{GP}(T_e^{GP})}{1-c_M^{GP}(T_e^{GP})} \tag{4}$$

Similarly for γ'' precipitation

$$Cu_{(1-\bar{c})}Be_{\bar{c}} \rightarrow rCu_{[1-c_M^{\gamma''}(T_e^{\gamma''})]}Be_{[c_M^{\gamma''}(T_e^{\gamma''})]} + q\,CuBe \tag{5}$$

where the γ'' composition was taken as CuBe [9] although it varies somewhat with temperature [16]; r is the number of moles of the Cu-rich matrix and q of CuBe

γ''-phase. Conservation of mass requires for copper

$$1 - \bar{c} = r[1 - c_M^{\gamma''}(T_e^{\gamma''})] + q \tag{6}$$

for beryllium

$$\bar{c} = r c_M^{\gamma''}(T_e) + q \tag{7}$$

Eqs. (6) and (7), after neglecting the term $c.c_M^{\gamma''}(T_e)$, yield

$$r = \frac{1 - \bar{c}}{1 - 2c_M^{\gamma''}(T_e)} \tag{8}$$

$$q = \frac{\bar{c} - c_M^{\gamma''}(T_e)}{1 - 2c_M^{\gamma''}(T_e^{\gamma''})} \tag{9}$$

Since $1 \gg 2c_M^{\gamma''}(T_e^{\gamma''})$, the denominators in Eqs. (3), (4), (8) and (9) can be approximated to unity. The values of $c_M^{GP}(T_e^{GP})$ and $c_M^{\gamma''}(T_e^{\gamma''})$ in Eqs. (4) and (9) were obtained from the solubility curves gathered by Strutt and Williams [18]. For consideration (b) mentioned above, the values of GP and γ'' precipitation heats can be obtained from the slope of the straight line through the data points of the plot of the logarithm of the (metastable) solid solubility versus the reciprocal temperature [24]. Table 2 summarizes the precipitation heat values obtained from a compilation of the data points given in Ref. [18], where values for γ' and γ are also included.

Therefore, the heat produced during GP precipitation is ΔH_c^{GP}

$$\Delta H_c^{GP} = \Delta H_p^{GP}[\bar{c} - c_M^{GP}(T_e^{GP})] \tag{10}$$

where ΔH_p^{GP} is the precipitation heat of GP zones. For γ'' the total precipitation heat $\Delta H_c^{\gamma''}$ per mole alloy is

$$\Delta H_c^{\gamma''} = \Delta H_p^{\gamma''}[\bar{c} - c_M^{\gamma''}(T_e^{\gamma''})] \tag{11}$$

where $\Delta H_p^{\gamma''}$ is the precipitation heat of γ''-phase.

Fig. 2 gives the calculated estimates for ΔH_c^{GP} and $\Delta H_c^{\gamma''}$ as well as the experimental values for the heat content $\Delta H_e^{(GP+\gamma'')}$ of effect A, as a function of heating rate ϕ. It can be seen that calculated values for γ'' precipitation are larger than for GP zone precipitation because: (1) the precipitation heat of γ''-phase is larger than that of the GP zones, and (2) beryllium atoms in γ''-phase precipitation outnumber those in GP-zone precipitation. Fig. 2 shows that the measured values for the heat content of effect A always lie between

Table 2
Precipitation heats of GP zones, and stable and metastable phases in Cu–Be alloys calculated from Ref. [18]

Phase/zone	Precipitation heat/(kJ per mol Be)
GP	16.00
γ''	28.10
γ'	34.13
γ	37.72

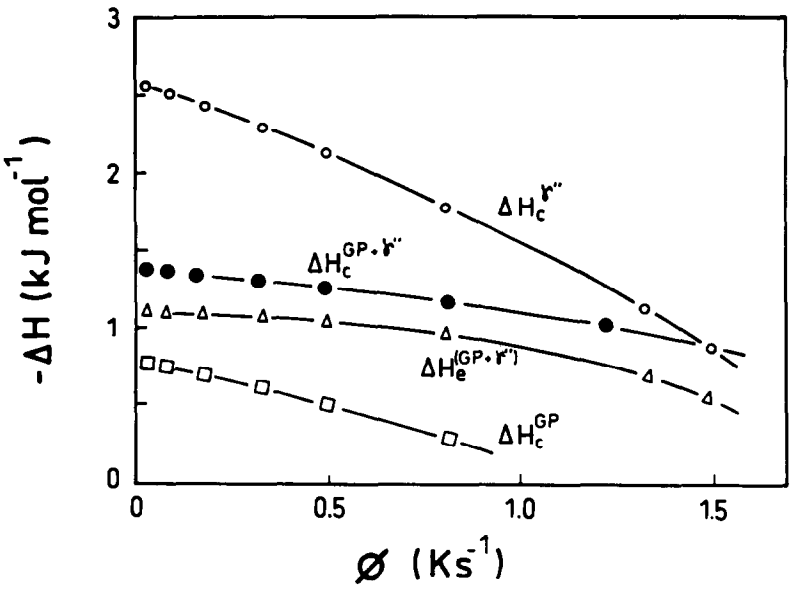

Fig. 2. Heat content $\Delta H_e^{(GP+\gamma'')}$ of effect A for quenched Cu–2Be, as a function of DSC heating rate. The calculated curves ΔH_c^{GP}, $\Delta H_e^{\gamma''}$ and $\Delta H_c^{(GP+\gamma'')}$ are also shown.

the limits calculated for GP and γ'' precipitations. At low heating rates, the experimental heat contents show enhanced GP precipitation. For high DSC heating rates, the experimental values correspond fairly well to the predominant γ'' formation, and thus beryllium precipitation then proceeds mainly as γ''-phase precipitation. The calculated values of event A which take into account the relative experimental importance of events A_1 and A_2 separately can be obtained by computing a combined precipitation heat, defined as

$$\Delta H_c^{(GP+\gamma'')} = \Psi \Delta H_c^{GP} + (1 - \Psi)\Lambda H_c^{\gamma''} \tag{12}$$

where the strengthening factor Ψ is

$$\Psi = \frac{\Delta H_c^{GP}}{\Delta H_e^{GP} + \Delta H_e^{\gamma''}} \tag{13}$$

ΔH_e^{GP} and $\Delta H_e^{\gamma''}$ being the heat contents of the deconvoluted thermal effects A_1 and A_2 respectively. The factor Ψ is a function of the heating rate. Both experimental and calculated plots are in fairly good agreement in Fig. 2. It is worth noticing that for GP zones, the interfacial energy and the energy related to the elastic strains can have a significant influence on the total energy of formation of the zones [25].

Since the creation of both strains and interfaces requires an energy input to the specimen, both strain and interfacial energy reduce the total amount of energy associated with the formation of zones. The importance of these contributions is

determined by the average size of the zones: the total formation energy of small zones contains relatively large strain and interfacial energy contributions. For Cu–Be alloys it was not possible to get estimates of these contributions, to the best of our knowledge.

The above analysis leads to the conclusion that heat event A corresponds to an overlapping sequential precipitation of GP zones and γ''-phase, which both nucleate and grow independently.

The right-hand side of Fig. 3 shows a schematic plot of Fig. 2. At a certain heating rate ϕ_1, corresponding values for $\Delta H_{c_1}^{GP}$, $\Delta H_{c_1}^{\gamma''}$ and $\Delta H_{e_1}^{(GP+\gamma'')}$ are obtained. On the left-hand side, the evolved heats are plotted in terms of the amount of beryllium precipitated Δc. Two straight lines with slopes ΔH_p^{GP} and $\Delta H_p^{\gamma''}$ drawn from the origin can be used to compute, after their intersection with the horizontals passing through $\Delta H_{c_1}^{GP}$ and $\Delta H_{c_1}^{\gamma''}$ respectively, the position of the $(\Delta H_{c_1}^{GP}, \Delta_{c_1}^{GP})$ and $(\Delta H_{c_1}^{\gamma''}, \Delta c_1^{\gamma''})$ data points. The intersection of the horizontal passing through $\Delta H_{e_1}^{(GP+\gamma'')}$ with the line connecting the above data points supplies the $(\Delta H_e^{(GP+\gamma'')}, \Delta c_1^{(GP+\gamma'')})$ point on the $(\Delta H, \Delta c)$ plane, based on linear interpolation. If the same procedure is repeated for other heating rates, the experimentally observed heat content of effect A can be determined as a function of the amount of beryllium atoms precipitated Δc. The resulting curve shown in Fig. 4 can be well approximated to a single straight line passing through the origin the slope of which gives the average heat of precipitation of beryllium atoms contained in the precipitates at the end of effect A: $\Delta H_p^{(GP+\gamma'')} = 21$ kJ mol^{-1} beryllium. This value is intermediate between the precipitation heats for GP zones and γ''-phase (16 and 28.1 kJ mol^{-1} beryllium).

Finally, concerning effect A, Fig. 5 shows the solvus of the combined precipitation related to effect A. Solid solubilities for GP zones and for γ''-phase (both obtained from Ref. [18]) are also shown.

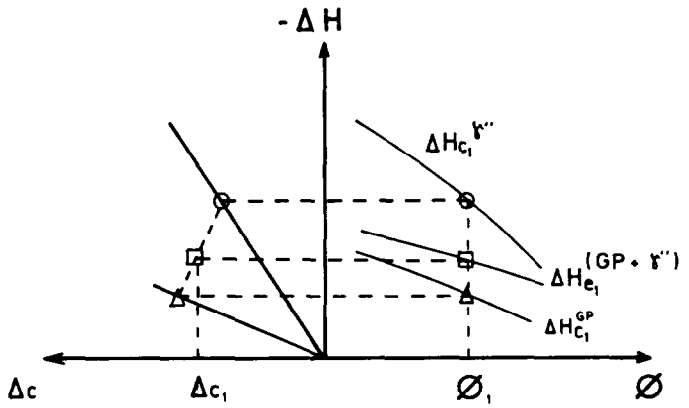

Fig. 3. Schematic plot of Fig. 2 shown on the right-hand side and its connection with the calculated and experimentally measured heats evolved during the combined precipitation of GP zones and γ''-phase (left-hand side) as a function of the amount of beryllium precipitated Δc.

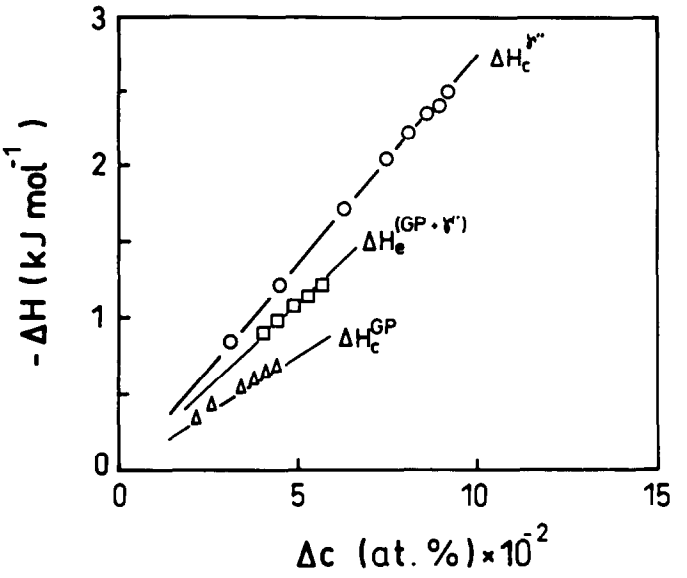

Fig. 4. Heat evolved during the combined GP-zone and γ''-phase precipitation effect as a function of Δc, the amount of beryllium precipitated. ΔH_c^{GP} and $\Delta H_c^{\gamma''}$ are calculated curves whereas the experimental curve $\Delta H_e^{(GP+\gamma'')}$ is based on the procedure used in Fig. 3.

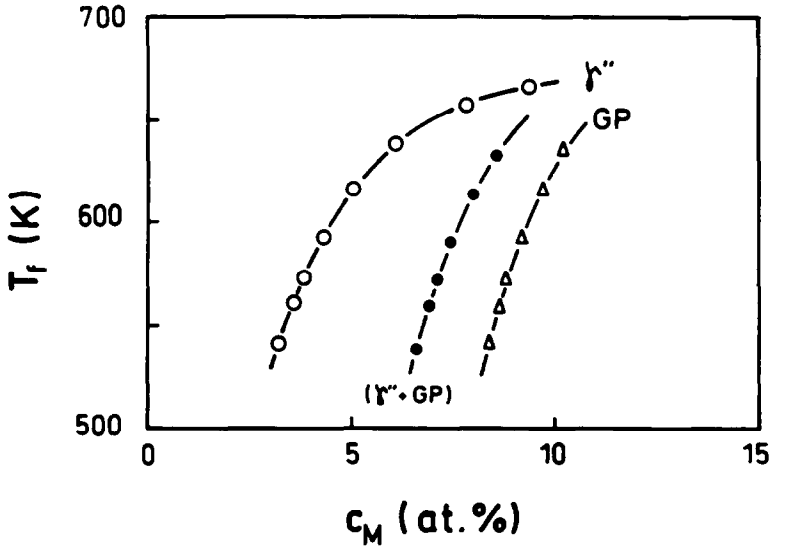

Fig. 5. Average matrix composition for the combined precipitation of GP zones and γ'' as a function of DSC heating rate. Solid solubilities for GP zones and γ''-phase are also shown.

3.3. Precipitation phenomena observed for effect B

As no endothermic effects occur during each DSC run, no dissolution of GP zones and γ'' takes place. Hence thermal events B_1 associated with γ', and B_2 associated with stable phase γ, cannot correspond to nucleation and growth processes but rather to transitions. In fact, if the procedure outlined in the previous section to verify the nature of effects A_1 and A_2 is now applied to events B_1 and B_2, then the experimentally measured heats $\Delta H_e^{(\gamma'+\gamma)}$ are always outside the calculated boundaries of γ' and γ precipitation for all heating rates and are far below the calculated heats $\Delta H_c^{(\gamma'+\gamma)}$. This feature is actually shown in Fig. 6. Thus, it must be concluded that exothermic effect B is attributed to transitions of less stable phases to γ'- and γ-phases.

The next task is identifying the phase or phases transformed from their primitive state into γ'- and γ-phases, and their relative contribution to such transitions. To this end, the heat evolved in the transition from a less stable to a more stable phase must first be calculated. For all the possible transitions considered, the heat contents are

$$\Delta H_c^{GP-\gamma'} = (\Delta H_p^{\gamma'} - \Delta H_p^{GP})[\bar{c} - c_M^{GP}(T_e^{GP})] \tag{14}$$

$$\Delta H_c^{\gamma''-\gamma'} = (\Delta H_p^{\gamma'} - \Delta H_p^{\gamma''})[\bar{c} - c_M^{\gamma''}(T_e^{\gamma''})] \tag{15}$$

$$\Delta H_c^{\gamma''-\gamma} = (\Delta H_p^{\gamma} - \Delta H_p^{\gamma''})[\bar{c} - c_M^{\gamma''}(T_e^{\gamma''})] \tag{16}$$

$$\Delta H_c^{\gamma'-\gamma} = (\Delta H_p^{\gamma} - \Delta H_p^{\gamma'})[\bar{c} - c_M^{\gamma'}(T_e^{\gamma'})] \tag{17}$$

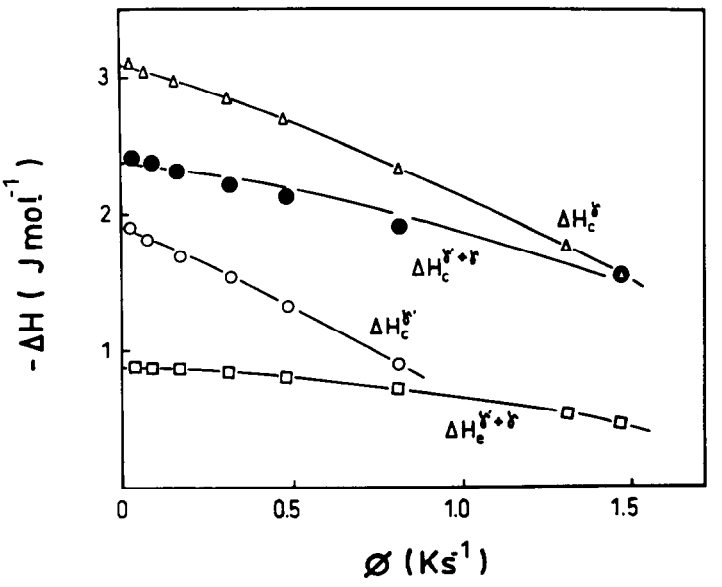

Fig. 6. Experimental heat content $\Delta H_e^{(\gamma'+\gamma)}$ of effect B for quenched Cu–2Be, as a function of the DSC heating rate. Calculated curves $\Delta H_c^{\gamma'}$, ΔH_c^{γ} and $\Delta H_c^{(\gamma'+\gamma)}$ for γ', γ and combined γ', γ precipitation are also shown. Notice that the experimental curve is outside the γ' and γ calculated boundaries.

where $\Delta H_c^{GP-\gamma'}$, $\Delta H_c^{\gamma''-\gamma'}$, $\Delta H_c^{\gamma''-\gamma}$ and $\Delta H_c^{\gamma'-\gamma}$ are the amounts of heat evolved during transitions GP→γ', γ''→γ', γ''→γ and γ'→γ respectively. The transition GP→γ was not considered since it leads to irrelevant results. All other terms of Eqs. (16)–(19) are already defined. If the calculated heats $\Delta H_c^{GP-\gamma'}$ and $\Delta H_c^{\gamma''-\gamma'}$ are plotted as a function of the heating rate and are compared with the experimental value $\Delta H_e^{\gamma'}$ measured after deconvolution of thermal effect B_1 shown in Fig. 7, it can be seen in Fig. 7(a) that the transition GP→γ' tends to be possible only at high heating rates, while the inverse is true for transition γ''→γ' shown in Fig. 7(b). In fact, both heat effects associated with GP and γ' (Fig. 1) decrease with increasing heating rate. It is then believed that both GP zones and γ''-phase contribute to the state with beryllium precipitated as γ'-phase. This is not surprising for the GP zones concerned, because the possibility of γ' formation inherited form GP zones has been experimentally observed and theoretically analysed, particularly when the zones have no chance to coarsen and begin to transform into γ'' [4]. This might also explain why the transition GP→γ'' is only possible at very low heating rates, as shown in Fig. 8 where $\Delta H_c^{GP-\gamma''}$ and $\Delta H_e^{\gamma''}$ are plotted as a function of ϕ. It can be observed that $\Delta H_c^{GP-\gamma''} \approx \Delta H_e^{\gamma''}$ for heating rates lower than 0.1 K s^{-1}. Figs. 9(a) and 9(b) show the calculated values of $\Delta H_c^{\gamma''-\gamma}$ and $\Delta H_c^{\gamma'-\gamma}$ and the experimental values for ΔH_e^{γ}. At high heating rates, the γ''→γ transition takes place (Fig. 9(a)). This feature is in agreement with an absence of GP zones and γ' for these high values of ϕ, as was shown in Fig. 1, such a mode of transition being, therefore, the only one possible. At very low heating rates, γ originates from the transition γ'→γ as observed in Fig. 9(b). The above results suggest that γ'' is partially involved in two of the observed transitions

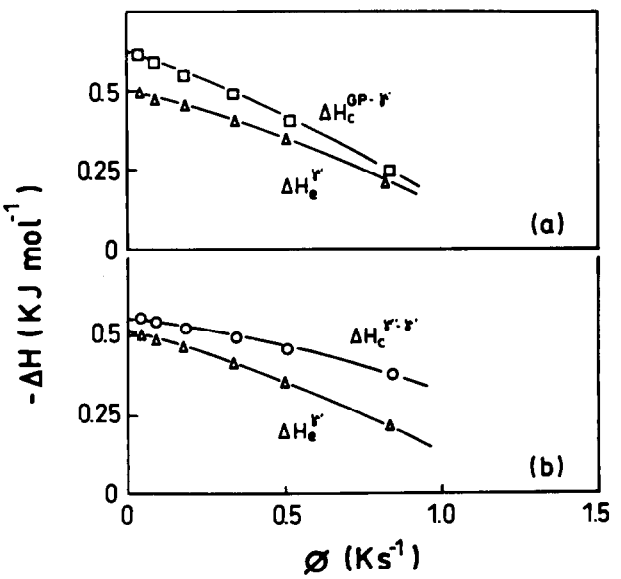

Fig. 7. Heat $\Delta H_e^{\gamma'}$ evolved during the transition to the state with γ'-phase as a function of DSC heating rate. The calculated values $\Delta H_c^{GP-\gamma'}$ and $\Delta H_c^{\gamma''-\gamma'}$ for the heat evolved during transitions GP→γ' and γ''→γ' are also shown in (a) and (b).

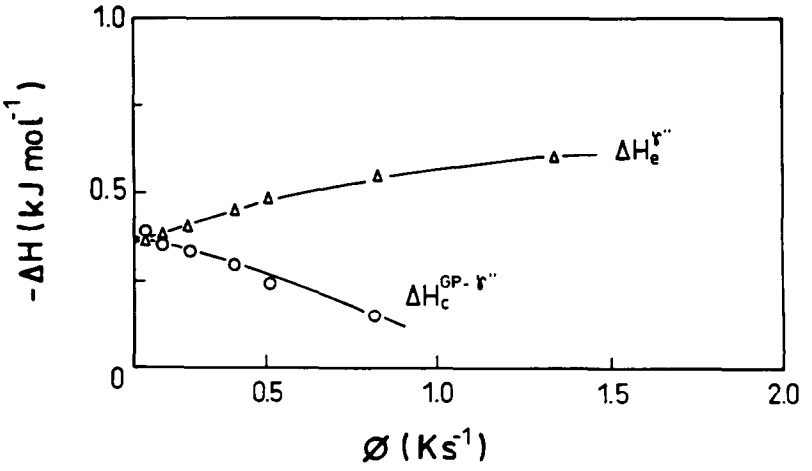

Fig. 8. Heat $\Delta H_e^{\gamma''}$ evolved during γ''-phase precipitation as a function of heating rate. The calculated heat-content curve $\Delta H_c^{GP-\gamma''}$ for the transition GP→γ'' is also shown. Notice that γ''-phase can be inherited from GP zones only at very low DSC heating rates.

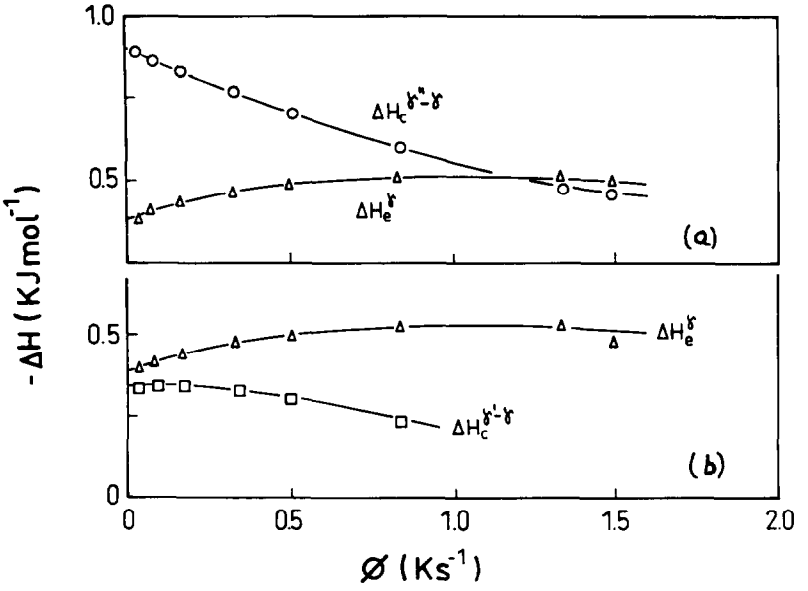

Fig. 9. Heat evolved during the transition to the state with γ-phase as a function of DSC heating rate. The calculated values $\Delta H_c^{\gamma''-\gamma}$ and $\Delta H_c^{\gamma'-\gamma}$ of the heat-content curves for transitions $\gamma''\rightarrow\gamma$ and $\gamma'\rightarrow\gamma$ are also shown in (a) and (b).

and thus one can assume that the transitions

$$\text{GP}, \gamma'' \rightarrow \gamma'$$

and

$$\gamma'', \gamma' \rightarrow \gamma$$

take place. They require that the heat effect associated with γ'' be partitioned into a fraction α contributing to the transition to the γ'-phase state, and a fraction $(1-\alpha)$ contributing to the transition to the γ-phase state. As the heat evolved in each thermal event of the DSC traces corresponds to a certain amount of the phase associated with the event, strengthening factors can be defined as follows

$$\psi^* = \frac{\Delta H_e^{GP}}{\Delta H_e^{GP} + \alpha \Delta H_e^{\gamma'}} \tag{18}$$

and

$$\Psi^* = \frac{(1-\alpha)\Delta H_e^{\gamma''}}{(1-\alpha)\Delta H_e^{\gamma''} + \Delta H_e^{\gamma'}} \tag{19}$$

and they ponderate the calculated heats of transition $\Delta H_e^{\gamma'}$ and ΔH_e^{γ} involved in achieving the states γ' and γ. By equating $\Delta H_e^{\gamma'} = \Delta H_e^{\gamma'}$ and $\Delta H_e^{\gamma} = \Delta H_e^{\gamma}$, the following expressions for such transitions can be written

$$\psi^* \Delta H_{GP}^{\gamma'} [\bar{c} - c_M^{GP}(T_e^{GP})] + (1-\psi^*)\Delta H_{\gamma''}^{\gamma'} [\bar{c} - c_M^{\gamma''}(T_e^{\gamma''}) = \Delta H_e^{\gamma'} \tag{20}$$

and

$$\Psi^* \Delta H_{\gamma''}^{\gamma'} [\bar{c} - c_M^{\gamma''}(T_e^{\gamma''})] + (1-\Psi^*)\Delta H_{\gamma'}^{\gamma} [\bar{c} - c_M^{\gamma'}(T_e^{\gamma'}) = \Delta H_e^{\gamma} \tag{21}$$

where

$$\Delta H_{GP}^{\gamma'} = \Delta H_p^{\gamma'} - \Delta H_p^{GP}$$

$$\Delta H_{\gamma''}^{\gamma'} = \Delta H_p^{\gamma'} - \Delta H_p^{\gamma''}$$

$$\Delta H_{\gamma''}^{\gamma'} = \Delta H_p^{\gamma'} - \Delta H_p^{\gamma''}$$

$$\Delta H_{\gamma'}^{\gamma} = \Delta H_p^{\gamma} - \Delta H_p^{\gamma'}$$

Values for ψ^* and Ψ^* are obtained from Eqs. (20) and (21) and are plotted as a function of ϕ in Fig. 10. Values for $\alpha(\psi^*)$ and $\alpha(\Psi^*)$ are shown in Fig. 11. It can be observed that $\alpha(\psi^*) = \alpha(\Psi^*)$ for all heating rates employed, thus confirming that the transitions formulated in Eqs. (20) and (21) are correct.

3.4. *Activation energy analysis*

Activation energies for thermal events associated with GP zones and γ'' formation as well as those for γ'- and γ-phase transformations were obtained by employing a variant of the Kissinger analysis [26], from the slope of a straight line through data points of a $\ln(T_f^2/\phi)$ vs. $1/T_f$ plot at certain transformation stages of the

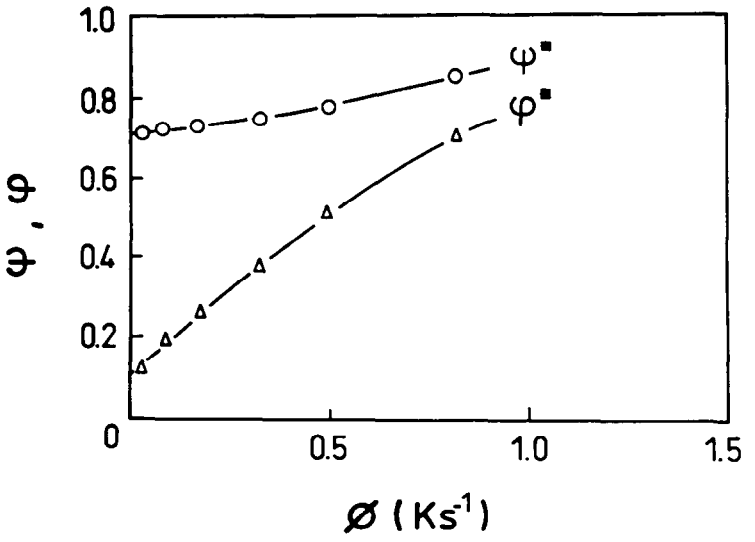

Fig. 10. Calculated factors ψ^* and Ψ^* from Eqs. (20) and (21) as a function of DSC heating rates.

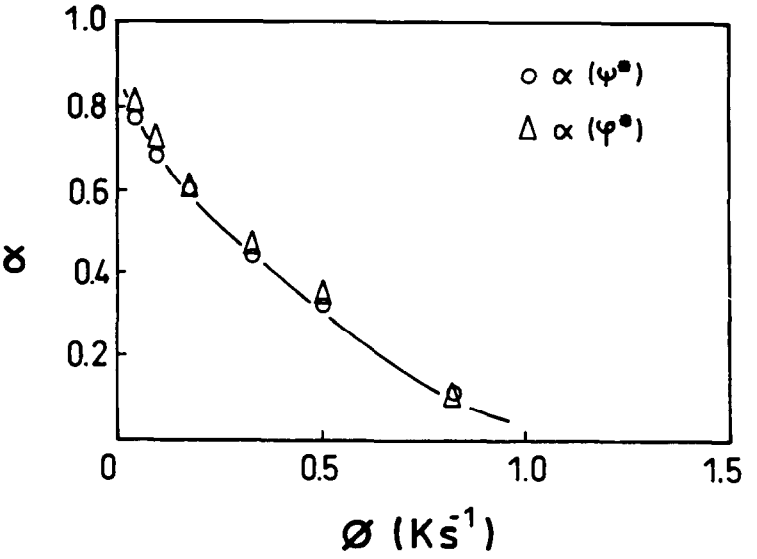

Fig. 11. Values for $\alpha(\psi^*)$ and $\alpha(\Psi^*)$ computed from Eqs. (18) and (19) as function of DSC heating rate.

deconvoluted peaks, T_f being the temperature for a fixed stage of transformation. Effective activation energies were calculated at four chosen transformation stages: at peak temperature, at 10%, at 50% and at 90% of the total heat evolved by effects A_1, A_2, B_1 and B_2. The values thus obtained did not differ significantly

in each case. Average computed values were as follows

$$E_a^{GP} = 0.94 \pm 0.07 \text{ eV}$$

$$E_a^{\gamma''} = 1.26 \pm 0.07 \text{ eV}$$

$$E_a^{\gamma'} = 1.31 \pm 0.08 \text{ eV}$$

$$E_a^{\gamma} = 1.69 \pm 0.10 \text{ eV}$$

where E_a^{GP}, $E_a^{\gamma''}$, $E_a^{\gamma'}$ and E_a^{γ} correspond to GP zones and γ''-, γ'-, γ-phases. It can be observed that the E_a^{GP} value is closely related to the value of vacancy migration, taken as about a half of 1.99 eV, the activation energy for beryllium diffusion in copper [17]. This means that GP-zone formation is mainly controlled by monovacancy migration and that less mobile complexes are likely to be absent. All other values, associated with the overall kinetics [30] of the different phases involved, are lower than the activation energy for beryllium diffusion in copper. As such diffusion can only proceed via a vacancy mechanism, significant amounts of excess vacancies are present in all these specimens.

Another reason for the lower values of the activation energies as compared to those of beryllium diffusion, is that such overall values are weighted averages of the activation energies controlling the kinetics of thickening and lengthening of the γ''-, γ'- and γ-plates. Although no specific data were found for Cu–Be alloys with respect to the above differences, at least in Al–Cu alloys the rate-dependent step for thickening appears to be ledge-formation of the broad surfaces of θ'-plates, whereas the rate-dependent step for lengthening was found to be pipe-diffusion. The activation energy for thickening was larger than for lengthening [27], but slightly lower than the activation energy for copper diffusion in aluminium [28]. If the same arguments are applied to copper–beryllium alloys, they strongly suggest that lengthening is relatively more important than thickening, as the phases considered become less stable. Typical transmission electron micrographs showing γ'- and γ-plates reveal this feature [15]. Hence, the increasing value obtained for activation energy as the phases become more stable (GP, γ'', γ' and γ) can be explained in this way.

It is interesting to notice that low heating-rate experiments show a small knee in the DSC traces preceding the transition to the γ'-phase (Fig. 1). An activation energy estimate for this knee using the above procedure yields 1.19 eV at 10% transformation after deconvolution, which equals the apparent activation energy for cell growth during discontinuous precipitation [13]. This result suggests the onset of discontinuous precipitation. At these temperatures, this precipitation at the grain boundaries is rapidly stopped by the γ'-plates lying within the grains. Fig. 12 shows a typical optical micrograph of a specimen heated at 0.333 K s^{-1} up to 700 K and then water-quenched. Discontinuous precipitation is observed at the grain boundaries; in the grain interiors a ripple structure revealing continuous precipitation can be discerned [15]. This reflects preferential alignment of precipitates along specific directions under the influence of tetragonal elastic distortions [27], or simply that more than one variant of orientations is present, such as occurs for α' elastically constrained precipitation in a hyper-eutectoid CuBe alloy [31, 32].

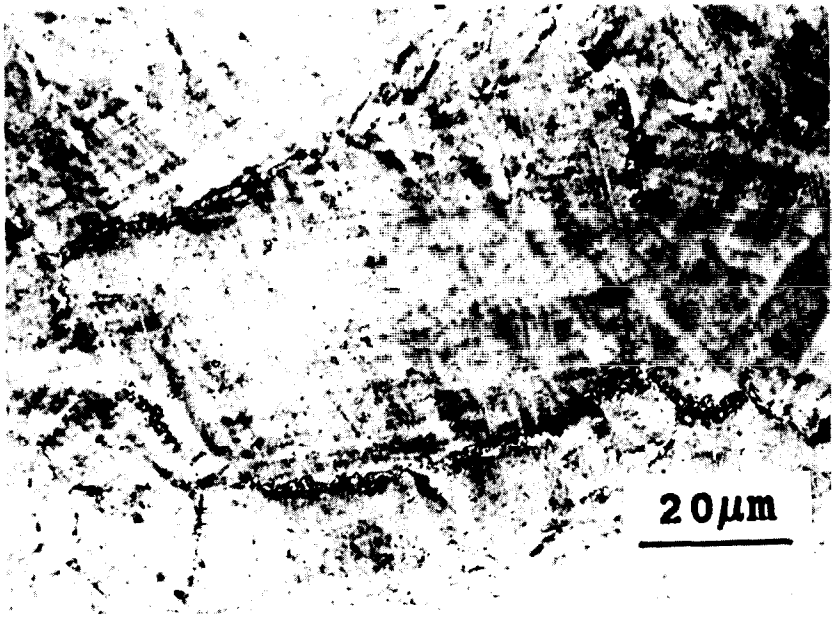

Fig. 12. Typical optical micrograph of a specimen heated at 0.333 K s^{-1} up to 700 K, and then water-quenched.

Also worth noticing is a small knee preceding thermal event A_1, associated with GP-zone formation in DSC traces appearing at low heating rates in Fig. 1. This effect might be due to the formation of small equiaxed clusters of beryllium that nucleate and grow as precursors prior to plate-like formation of GP zone [4, 8].

To summarize, the non-isothermal precipitation sequence in Cu–2Be is shown schematically in Fig. 13 where γ_{disc} and γ_{cont} are discontinuous and continuous precipitations of γ.

4. Conclusions

Quenched Cu–2Be alloys subjected to non-isothermal DSC runs using a wide range of heating rates led to the following findings:

(1) At low heating rates, GP zones and γ''-phase nucleate and grow independently. The amount of GP zone decreases with increasing heating rate and is even hindered at high heating rates due to inefficiency resulting from excess vacancies.

(2) The heat content of the combined GP/γ''-phase precipitation effect appears to be proportional to the number of beryllium atoms precipitated, yielding an average value for the heat of beryllium precipitation of 21 kJ mol^{-1} beryllium.

(3) The γ''-phase can be inherited from GP zones only at very low heating rates.

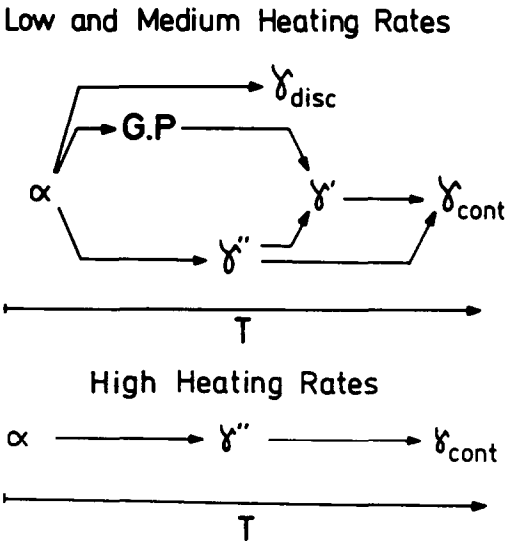

Fig. 13. Schematic representation of the phases involved with increasing temperature in non-isothermal precipitations in quenched Cu–2Be.

(4) The γ''-phase contributes partially to the transitions to states with γ'- and γ-phases.

(5) Transition to the state with γ'-phase arises from the combined contribution of GP zones and γ''.

(6) Transition to the state with γ-phase arises from the combined contribution of γ''- and γ'-phases.

(7) At the highest heating rates, the state with γ'-phase is absent and transition to the state with γ-phase arises completely from γ''-phase.

(8) The apparent activation energy of GP-zone formation is consistent with the activation energy for vacancy migration. Apparent activation energies associated with γ''-, γ'- and γ-phases show increasing values respectively. Two factors can influence this feature: the mobility of the dissolved atoms and the growth direction (either normal, or perpendicular to the plates). The relative importance of these factors may depend on temperature.

Acknowledgements

The authors express their gratitude to Professor Jaroslav Šesták for many valuable suggestions. They are also indebted to the Fondo Nacional de Desarrollo Científico y Tecnológico (FONDECYT), Proyect No. 1950566, for financial support and to the Instituto de Investigaciones y Ensayes de Materiales (IDIEM), Universidad de Chile, for the facilities given for this research work.

References

[1] K. Shimizu, Y. Mikami, H. Mitani and K. Otzuka, Trans. Jpn. Inst. Met., 12 (1971) 206.
[2] S. Yamamoto, M. Matsui and Y. Murakami, Trans. Jpn. Inst. Met., 12 (1971) 159.
[3] W.H. Bonfield and B.C. Edwards, J. Mater. Sci., 9 (1974) 398.
[4] R.J. Rioja and D.E. Laughlin, Acta Metall., 28 (1980) 1301.
[5] J.M. Pelletier, G. Vigier, C. Mai and R. Borrelly, Acta Metall., 31 (1983) 1491.
[6] Y.M. Koo, J.B. Cohen, S.M. Shapiro and L.E. Tanner, Acta Metall. 36 (1988) 591.
[7] Y.M. Koo and J.B. Cohen, Acta Metall., 37 (1989) 1295.
[8] J.B. Cohen, Metall. Trans., 23A (1992) 2685.
[9] A.G. Khachaturyan and D.E. Laughlin, Acta Metall. Mater., 38 (1990) 1823.
[10] A. Yamamoto, R. Nozato, T. Morimoto and H. Tsubakino, Mater. Trans. JIM, 34 (1993) 312.
[11] A. Yamamoto and H. Tsubakino, Scripta Metall. Mater., 31 (1994) 787.
[12] W. Bonfield and B.C. Edwards, J. Mater. Sci., 9 (1974) 409.
[13] T. Tsubakino, R. Nozato and H. Hagiwara, Trans. Jpn. Inst. Met., 22 (1981) 153.
[14] H. Tsubakino, R. Nozato and A. Yamamoto, J. Mater. Sci., 26 (1991) 2851.
[15] H. Tsubakino, R. Nozato and A. Yamamoto, Mater. Sci. Technol., 9 (1993) 288.
[16] L.G. Garrilenko, B.M. Mogutnov and L.A. Shvartsman, Phys. Met. Metall., 27 (1969) 116.
[17] T. Ohshima and K. Hirano, Themochim. Acta, 93 (1985) 645.
[18] A.J. Strutt and D.B. Williams, Philos. Mag., 67A (1993) 1007.
[19] M.J. Starnik and P. Van Mourik, Metall. Trans., 22A (1991) 665.
[20] M.J. Starnik and P. Van Mourik, Mater. Sci. Eng., A156 (1992) 183.
[21] A. Varschavsky and E. Donoso, Mater. Sci. Eng., A145 (1991) 95.
[22] A. Varschavsky, Thermochim. Acta, 203 (1992) 391.
[23] A. Varschavsky and M. Pilleux, Mater. Lett., 17 (1993) 364.
[24] M. van Rooyen and E. J. Mittemeijer, Metall. Trans., 20A (1989) 1207.
[25] A.M. Zahra, M. Laffitte and M. Winterberger, Mem. Sci. Rev. Metall., 74 (1977) 561.
[26] E.J. Mittemeijer, Liu Chang, P.J. van der Schaaf, C.M. Brakman and B.M. Korevaar, Metall. Trans., 19A (1988) 925.
[27] H.I. Aaronson and C. Laird, Trans. AIME, 242 (1968) 1437.
[28] L.F. Mondolfo, Aluminium Alloys: Structure and Properties, Butterworths, London, 1976.
[29] R.J. Rioja and D.E. Laughlin, in H.I. Aaronson, D.E. Laughlin, R. Sekerka and C.M. Wayman (Eds.), Proceedings of an International Conference on Solid–Solid Phase Transformations, The Metallurgical Society of AIME, Warrandale, Pennsylvania, USA, 1982, p. 1089.
[30] J. Šesták and J. Málek, Solid State Ionics, 63–65 (1993) 245.
[31] B. Cheong, K. Hono and D.E. Laughlin, Metall. Trans., 24A (1993) 2605.
[32] B. Cheong, K. Hono and D.E. Laughlin, Acta Metall. Mater., 42 (1994) 2387.